

Short Title: Proteomic response to antibiotics

**Decreased antibiotic susceptibility driven by global remodeling of the *Klebsiella pneumoniae* proteome**

Sarah L. Keasey<sup>a,b,†</sup>, Moo-Jin Suh<sup>b,†,\*</sup>, Sudipto Das<sup>c</sup>, Candace D. Blancett<sup>d</sup>, Xiankun Zeng<sup>d</sup>,  
Thorkell Andresson<sup>c</sup>, Mei G. Sun<sup>d</sup>, and Robert G. Ulrich<sup>b,1</sup>

<sup>a</sup>Department of Biological Sciences, University of Maryland Baltimore County, Baltimore, Maryland, USA; <sup>b</sup>Molecular and Translational Sciences Division, U.S. Army Medical Research Institute of Infectious Diseases, Frederick, Maryland, USA. <sup>c</sup>Laboratory of Proteomics and Analytical Technologies, Leidos Biomedical Research, Frederick National Laboratory for Cancer Research, NCI-Frederick, Frederick, Maryland, USA. <sup>d</sup>Pathology Division, U.S. Army Medical Research Institute of Infectious Diseases, Frederick, Maryland, USA.

<sup>†</sup>Authors contributed equally to this work

\*ORCID :000-003-003-393X

<sup>1</sup>Corresponding author: robert.g.ulrich.civ@mail.mil

## Abbreviations

CFU	colony forming units
CPS	capsular polysaccharide
Ct	time to detectable growth
DC	doxycycline
EM	electron microscopy
ESBL	extended spectrum beta-lactamase
LB	luria-bertani
MDK	minimum duration of killing
MIC	minimum inhibitory concentration
PCA	principal
PMF	proton motive force
SM	streptomycin
TCA	tricarboxylic acid

## Abstract

Bacteria can circumvent the effect of antibiotics by transitioning to a poorly understood physiological state that does not involve conventional genetic elements of resistance. Here we examine antibiotic susceptibility with a Class A  $\beta$ -lactamase+ invasive strain of *Klebsiella pneumoniae* that was isolated from a lethal outbreak within laboratory colonies of *Chlorocebus aethiops sabaeus* monkeys. Bacterial responses to the ribosomal synthesis inhibitors streptomycin and doxycycline resulted in distinct proteomic adjustments that facilitated decreased susceptibility to each antibiotic. Drug-specific changes to proteomes included proteins for receptor-mediated membrane transport and sugar utilization, central metabolism, and capsule production, while mechanisms common to both antibiotics included elevated scavenging of reactive oxygen species and turnover of misfolded proteins. Resistance to combined antibiotics presented integrated adjustments to protein levels as well as unique drug-specific proteomic features. Our results demonstrate that dampening of *Klebsiella pneumoniae* susceptibility involves global remodeling of the bacterial proteome to counter the effects of antibiotics and stabilize growth.

## Introduction

As a commensal Gram-negative bacterium that colonizes mucosal surfaces of the gastrointestinal and respiratory tracts, *K. pneumoniae* readily adheres to medical devices, thereby increasing risk of infection for patients undergoing procedures with reused or inserted medical equipment (1, 2), and immunocompromised individuals are especially vulnerable (3). The emergence of more-virulent and invasive *K. pneumoniae* strains (4) has broadened the susceptible population to include individuals who are healthy and non-immunocompromised. Moreover, the failure of first-line broad-spectrum therapies against clinical isolates is leading to an increase of infections that are chronic and recalcitrant to treatment (3). Recently, an outbreak of carbapenem-resistant *K. pneumoniae* occurred at the Clinical Center of the U.S. National Institutes of Health, causing the deaths of 11 of 18 affected patients (3). Moreover, an outbreak of chronic and lethal infections that occurred within laboratory primate colonies of *Chlorocebus aethiops sabaeus* (5, 6) was caused by a hypermucoviscous and invasive strain of *K. pneumoniae* V513 (*KpV513*). Animals infected by the *KpV513* strain did not respond to antibiotics, and this outbreak provides a primate model to better understand drug interactions with this emerging bacterial pathogen.

Bacteria can survive antibiotic treatment through acquisition of genetically encoded elements that confer specific resistance or by transitioning to a phenotypic state of resistance that can be experimentally demonstrated by culturing with antibiotic levels that are below the minimum inhibitory concentration (sub-MIC). Further, the termination of antibiotic therapy for chronic infections (7-9) often results in disease relapse due to the resurgent growth of bacteria that survived antibiotic exposure. Previous studies have reported that susceptible Gram-negative bacteria that survive antibiotic treatment exhibit stochastic variations in levels of ppGpp(10) and

ATP(11) that coincide with slow growth or states of dormancy. However, many factors must come into play for infection to continue after antibiotic treatment, and it is possible that additional features can be detected by proteomic-level studies of antibiotic responses. Here we examined population and proteomic dynamics of *KpV513* under experimental conditions that replicate phenotypic resistance to disparate classes of drugs.

## Materials and Methods

**Microscopy.** For immunohistochemistry, formalin-fixed and paraffin embedded (FFPE) tissue sections were de-paraffinized using xylene and a series of ethanol washes. After the sections were treated with hydrogen peroxide blocking reagent blocks signal from endogenous peroxidases, the sections were blocked and incubated with rabbit anti- *Klebsiella pneumoniae* polyclonal antibody (1:2000, Thermofisher Scientific, Waltham, MA, USA) for 2 h at room temperature. Sections were visualized using a horseradish peroxidase-labeled polymer, Envision + system (anti-rabbit) (Agilent, Santa Clara, CA, USA) subjected to reaction with the chromogen diaminobenzidine. For immunofluorescence, formalin-fixed and paraffin embedded tissue sections were deparaffinized using xylene and a series of ethanol washes. After 0.1% Sudan black B (Sigma-Aldrich, St. Louis, MO, USA) treatment to eliminate autofluorescent backgrounds, the sections were heated in citrate buffer (pH 6.0) for 15 minutes to reverse formaldehyde crosslinks. After rinses with PBS (pH 7.4), the sections were blocked with PBS containing 5% normal goat serum overnight at 4°C, and incubated with rabbit anti- *Klebsiella pneumoniae* polyclonal antibody (1:2000, Thermofisher Scientific) for 2 h at room temperature. After rinses with PBS, the sections were incubated with secondary Alexa Fluor 568 conjugated goat anti-rabbit antibody for 1 h at room temperature. Sections were cover slipped using

Vectashield mounting medium with DAPI (Vector Laboratories, Burlingame, CA, USA). Images were captured on a Zeiss LSM 780 confocal system (Jena, Germany) and processed using ImageJ software.

**Electron Microscopy.** Bacteria were grown to mid-log phase ( $OD_{600} = 0.5$ ) in SM, DC or untreated control medium. The cells were harvested by centrifugation at  $5000\times g$  for 10 min at  $4^{\circ}C$ . Bacteria were fixed at room temperature for 1 h in EM primary fixatives of 2.5% formaldehyde and 2.5% glutaraldehyde in 0.1 M sodium cacodylate (pH 7.4) buffer. For transmission electron microscopy, the fixed bacteria were washed three times for 10min each in 0.1M sodium cacodylate buffer, incubated for 1 h in 1% osmium tetroxide in 0.1 M sodium cacodylate buffer, and washed with distilled water for 10 min. The samples were stained for 1 h in 1% uranyl acetate, dehydrated in an ethanol series of 30%, 50%, 75% and 95%, successively, for 10 min each, followed by three 10 min washes in 100% ethanol and two 10 min washes in propylene oxide. Samples were infiltrated with agitation at room temperature in well-mixed 50% v/v propylene oxide/Epon812 (Electron Microscopy Sciences, Cat#RT14120) for 1 h, followed by 100% Epon 812 three times for 1 h each. The samples were placed in an oven and allowed to polymerize at  $60^{\circ}C$  for 24 hr. Thin sections (approximately 80nm) were collected and pre-stained with 1% uranyl acetate and Sato lead before examination in a JEOL 1011 transmission electron microscope at 80kv. Digital images were acquired using AMT camera system. For scanning electron microscopy, the fixed bacteria were transferred to filter membranes under vacuum, and washed and dehydrated as described above, excluding the propylene oxide wash steps. The prepared samples were transferred to a critical point dryer to reach critical point dryness, mounted on specimen stubs, and sputter coated with 6 nm iridium. The samples were

loaded into Zeiss Sigma field emission scanning electron microscope using 2kV InLens secondary electron detector, and digital images were acquired using SmartSEM software. Two biological replicates were performed for each condition.

**Bacterial cultures and antimicrobial susceptibility testing.** Bacterial cultures were grown at 37°C with 250 rpm shaking in Luria-Bertani (*KpV513*, clinical isolates of *K. pneumoniae*, *Escherichia coli*, *Acinetobacter baumannii*) or heart infusion (*Yersinia pestis*) broth with aeration. After 16h, bacteria were diluted 1:100 in culture broth and grown to the mid-log phase ( $OD_{600} \sim 0.5$ ) twice to synchronize growth. Plating of serially diluted cultures established that  $5 \times 10^8$  colony forming units (cfu) were present in mid-log phase cultures. Determination of antibiotic minimum inhibitory concentrations (MIC) was performed as previously described(12), in microplate format. Absorbance of each microplate well (200  $\mu$ L culture) at 600 nm was monitored using a Bioscreen CTM Automated Microbiology Growth Curve Analysis System (Growth Curves USA, Piscataway NJ). The MIC endpoint was determined as the lowest concentration of antibiotic at which there was no visible growth after 20 hr. For isolation of untreated and antibiotic treated cells, replicate wells ( $n = 6$ ) of *KpV513* bacteria in culture  $\pm$  antibiotic at 50% of the MIC concentration ( $MIC_{50}$ ) were harvested at mid-log phase by centrifugation at  $5000 \times g$  for 10 min at 4°C. Supernatant absorbance was recorded and cell pellets were stored at  $-80^\circ\text{C}$ . Six biological replicates were performed for each condition, except for the combination treatment of streptomycin + doxycycline, which was performed in triplicate. Using the string test on doxycycline-treated colonies, which exhibited a distinct mucoid phenotype, hypermucoviscosity was defined by formation of viscous strings  $> 5\text{mm}$  long (13).

For cyclic administration of antibiotics, untreated or antibiotic treated *KpV513* were treated at a low level of detection (i.e. at their calculated  $C_t$ , see below) with MIC<sub>50</sub> antibiotics.

**Acid production and glucose utilization.** *K. pneumoniae* were cultured untreated or with antibiotic(s) at the MIC<sub>50</sub>, harvested during mid-exponential growth, and centrifuged at 5000 x g for 10 min to pellet cells. The pH indicator bromothymol blue (0.03%) was added to culture supernatants (n = 3), and absorbance at 620nm (blue, pH  $\geq$  7.2) and 425nm (yellow, pH  $\leq$  6), which are peak absorption wavelengths of the deprotonated and protonated forms of bromothymol blue, respectively, were recorded. Glucose utilization was assessed under hypoxic and aerobic conditions using Hugh and Leifson's oxidation fermentation basal medium (pH 7.1) with glucose as the sole carbohydrate source. Cell pellets were washed twice in antibiotic-free broth and inoculated as stabs into two tubes of oxidative fermentative medium media. One tube from each pair was overlaid with mineral oil as a barrier to oxygen diffusion (hypoxic conditions). Tubes were incubated at 37°C for 5 h and levels of acid production from glucose metabolism were recorded as the percentage of medium within the tube that changed color from blue (pH 7.1) to yellow (pH 6).

**Growth curve analysis.** The time to detectable growth,  $C_t$ , was calculated by fitting an exponential curve to the initial phase of growth and solving for x at  $y = 10^{-6}$ . For predictions using the discrete dynamical systems model, measurements of bacterial population density are denoted by  $D$ , where  $D_0$  is the starting cell density and  $D_t$  reflects bacterial density at subsequent time points  $t$ . Population density was recorded every 15 min, and  $t$  denotes rescaled time, such that each 15 min interval represents one unit of time ( $t = 0, 1, 2, 3, \dots$ ; for  $t = 3$ , the



corresponding time in the experiment is  $3 \times 15 \text{ min} = 45 \text{ min}$ ). The change in population density ( $D_{t+1} - D_t$ ) with time  $((t+1) - t)$  exhibited a parabolic pattern, in which the population change increased faster than linearly, indicating that the doubling rate of bacteria was greater than the measurement time interval (15 min). Assuming constant rates of cellular division, we expect the population change ( $D_{t+1} - D_t$ ) to be a fixed fraction of the population  $D_t$ , and the model should be of the form

$$D_{t+1} - D_t = rD_t, \quad (\text{eq.1})$$

where  $r$  is a constant that reflects the proportion of cells dividing during each time interval. We plotted population density versus population change for each time interval during the early phase of detectable growth. The resulting linear line intersects the origin and the slope of the line gives  $r$ . Here,  $15/r$  yields the dividing time in minutes. In function form, (eq.1) becomes

$$f(D_t) = (1/r) \times D_t = D_{t+1}, \quad (\text{eq.2})$$

and iterating  $f$ , we can express the general solution of the discrete dynamical system for the initial condition  $D_o$  as

$$D_t = D_o \times (1/r)^t. \quad (\text{eq.3})$$

To estimate the proportion of cells that initiated resurgent growth,  $D_o$  of untreated *KpV513* was calculated using (eq.3). Because *KpV513* cultures were serially diluted such that  $\sim 200\text{cfu}$  were inoculated into each microwell, we validated our mathematical model by comparing the theoretical  $D_o$  to the number of cfu experimentally added to culture. Over replicate experiments ( $n = 6$ ),  $D_o = 200 \pm 25\text{cfu}$ . Next, because antibiotic-treated *KpV513* cultures were inoculated with the same stock of serially diluted cells, we used (eq. 3) to estimate the theoretical  $D_t$  of treated cultures at the untreated  $C_t$ , using  $r$  from growth of treated cells and  $D_o$  from untreated cultures.

Finally, again using (eq.3), we could estimate  $D_o$  of treated cultures based on the treated theoretical  $D_t$  and  $r$ .

To describe the effect of decreasing growth rates on culture capacity, we fit a logistic model to measurements of culture absorbance approaching stationary phase. The relative population change was reduced as population size increases, eventually approaching zero as the environmental carrying capacity was reached. Therefore, the relative population change was proportional to the unused carrying capacity, such that

$$\frac{D_{t+1} - D_t}{D_t} = r \frac{(1 - D_t)}{M}. \quad (\text{eq.4})$$

For decaying rates of growth, we plotted the relative population change  $(D_{t+1} - D_t) / D_t$  versus the population size  $D_t$ . If  $x = D_t$  and  $y = (D_{t+1} - D_t) / D_t$ , then

$$y = r(1 - x/M) = r - (r/M)x, \quad (\text{eq.5})$$

and the data should lie along a line with slope  $-r/M$  and y-intercept of  $r$ . We calculated  $M$ , which reflects  $M_{initial}$  because it is based on the maximum capacity achieved prior to declining growth rates, and compared it to  $M_{decay}$ , which is the experimentally observed maximum culture density.

Growth curves were derived and integrated for phase-portrait graphs (Fig. 4) using Origin Pro Software.

**Imaging mass spectrometry.** MALDI imaging MS was performed using a Solarix dual source Fourier transform-ion cyclotron resonance (FT-ICR) mass spectrometer (Bruker Daltonics, Billerica, MA) with a SmartBeam II laser operating at 1kHz, a laser spot size of 25  $\mu\text{m}$ , and a raster width of 200  $\mu\text{m}$  for general profiling. Spectra in positive ion mode were generated using 100 laser shots at a frequency of 1 kHz. Ion images for tissue sections were acquired in 4 h at a

peak resolution of ~125,000 (FWHM,  $m/z$  400). Following MS analysis, data was loaded into FlexImaging Software focusing on the  $m/z = 700\text{--}3500$  range and reduced to 0.98 ICR Reduction Noise thresholds. All data were normalized by root mean squares.

**Sample Preparation for shotgun proteomics.** *KpV513* cell pellets were suspended and sonicated for 200s (10s on, 10s off, 10 runs at 20W) in an ice bath of 1 ml ice-cold 25 mM Tris-HCl (pH 7.4, added lysozyme, DNase I, Protease Inhibitor). Sonicated bacterial suspensions were centrifuged at  $5000\times g$  at  $10^{\circ}\text{C}$  for 20 minutes. Supernatants were analyzed by SDS-PAGE (Bio-Rad, Hercules, CA) followed by Coomassie stain, and total protein concentration was determined using the Bradford protein assay (Bio-Rad, Hercules, CA). 100  $\mu\text{g}$  of total cell lysate was used to generate tryptic digest using the ‘filter-aided sample preparation’ (FASP) protein digestion method(14). *KpV513* proteins in buffer (50 mM ammonium bicarbonate, 8 M urea) were reduced by dithiothreitol and alkylated with 20 mM iodoacetamide in the dark for 1 hr. After diluting into 1 M urea, alkylated proteins were digested with trypsin (1:100 w/w, Promega, Madison, WI) at  $37^{\circ}\text{C}$  for 12 h and cleaned with Stage-Tip prior to 1D-LC-MS/MS(15).

**Liquid chromatography and tandem mass spectrometry.** All LC-MS/MS analysis was performed on both Orbitrap Elite and Fusion Classic mass spectrometers (Thermo Scientific, San Jose, CA). 100 ng of desalted tryptic protein digest was loaded onto Acclaim™ PepMap™ 100  $\text{C}_{18}$  LC column (Thermo Scientific, CA) using a Thermo Easy nLC 1000 LC system (Thermo Scientific, CA) connected online with Orbitrap Fusion Classic mass spectrometer. After sample injection, the peptides were eluted using LC methods, running 1% to 35% LC gradients of aqueous, formic acid /acidified acetonitrile over 100 min at a flow rate of 300 nl/min. The Fusion

mass spectrometer was operated in a data dependent mode in which each full MS scan was followed by 20 data-dependent MS/MS scans. Voltage setting at the nano-spray was set at 2.3 kV for stable spray. Each MS<sup>1</sup> scan was performed in the Orbitrap at a resolution of 60,000, with maximum injection time of 50 ms and AGC target set at  $2 \times 10^5$  counts. For MS<sup>2</sup> scan, a normalized collision energy setting of 29 was used with a maximum injection time of 75 ms and AGC target set to  $1 \times 10^4$  counts.

For Orbitrap Elite MS, the desalted tryptic protein digest was loaded onto an Ultimate 3000 HPLC (Thermo Fisher Scientific) with a pulled-tip 75  $\mu\text{m} \times 15$  cm C<sub>18</sub> column (New Objective, PicoFrit column) at a flow rate of 300 nl/min. The peptides were eluted using LC methods as described above. Voltage settings at the nano-spray source were optimized at 2.0 kV to ensure stable fine spray. The cycles of 10 data-dependent MS/MS scans per MS<sup>1</sup> scan were performed. For all collision-induced dissociation (CID) scans, a normalized collision energy of 30 was used, the maximum inject time was 100 ms and maximum ion counts sat to  $1 \times 10^4$  counts for MS<sup>2</sup>. Two technical replicates were performed for each biological replicate. Two biological samples were also tested for comparison of data between two mass spectrometers (Fusion and Elite).

**Protein identification and quantification.** Raw MS data were collected and analyzed using Proteome Discoverer (version 2.2, Thermo Scientific) with Sequest HT search software and MaxQuant (version 1.6.0.1) incorporated with the Andromeda search engine. Each search engine was supplied with a database comprising comprehensive *K. pneumoniae* protein sequences (downloaded on 9 July 2016, 5126 proteins, Taxonomy 272620) combined with common contaminants proteins. Mass tolerance settings were as follows: fragment ion mass 0.6 Da, parent

ion tolerance 10 ppm (Sequest); precursor ion mass 10 ppm and fragment ion mass 20 ppm (MaxQuant). Search settings included trypsin as the digestion enzyme, minimal peptide length of six amino acids, and a maximum of two missed cleavage sites. Carbamidomethylation of cysteine was set as a fixed modification, and N-terminal protein acetylation and methionine oxidation as variable modifications. The maximum false discovery rate (FDR) was set at 1%. Two unique peptides were selected for a protein identification using Sequest. This approach was used in initial analysis stages to ensure that raw datasets had sufficient proteome depth. Combining data files representing two LC-MS/MS replicates for each biological replicate, the label-free quantitation (LFQ) values derived from the LFQ algorithm in MaxQuant were used for quantitative analysis. Default settings for quantification based on MS peak integration and for normalization among all datasets were accepted. Protein isoforms that could not be discriminated based on unique peptides were reported as a single protein group. Proteins not present in at least 15% of the samples were removed. We used abundance distribution-based imputation (ADI) to replace missing values (MVs) (16, 17). ADI is a randomized imputation method based on normal abundance distribution to simulate a typical abundance region for MVs if experimentally measured (Supplemental File S4).

**Experimental design and statistical rationale.** For statistical analyses, proteomic data were used from six biological replicates of LC-MS/MS analyses for each experimental group except the combination treatment of streptomycin + doxycycline, which was performed in triplicate. A non-parametric (Wilcoxon-Mann-Whitney) test was used to distinguish statistically significant changes between antibiotic-treated and the untreated control *KpV513* cultures. Proteins with P-value < 0.05 and  $\pm 2$  fold change were considered significant and differentially abundant. A

principal component analysis (PCA) was performed in Perseus software, using a minimum peptide cutoff = 20, only proteins present in at least 80% of the spot maps, and a Benjamini-Hochberg procedure with a significance level of 0.05. Differentially abundant proteins in the proteomes of SM- or DC-treated *KpV513* were mapped to cellular pathways using the KEGG database ([www.genome.jp/kegg/pathway.html](http://www.genome.jp/kegg/pathway.html)).

### Data Availability

The mass spectrometry proteomics data have been submitted to the ProteomeXchange Consortium via the PRIDE data repository (18) with the dataset identifiers PXD005587, PXD009175, and PXD010244. In addition, data sets can be visualized in MS-viewer using the following URLs:

#### *Untreated Kp proteome*

Search key: lyhdoz5qdr

URL: [http://msviewer.ucsf.edu/prospector/cgi-bin/mssearch.cgi?report\\_title=MS-Viewer&search\\_key=lyhdoz5qdr&search\\_name=msviewer](http://msviewer.ucsf.edu/prospector/cgi-bin/mssearch.cgi?report_title=MS-Viewer&search_key=lyhdoz5qdr&search_name=msviewer)

#### *SM-treated Kp proteome*

Search key: ljjmcsbhke

URL: [http://msviewer.ucsf.edu/prospector/cgi-bin/mssearch.cgi?report\\_title=MS-Viewer&search\\_key=ljjmcsbhke&search\\_name=msviewer](http://msviewer.ucsf.edu/prospector/cgi-bin/mssearch.cgi?report_title=MS-Viewer&search_key=ljjmcsbhke&search_name=msviewer)

#### *DC-treated Kp proteome*

Search key: kqlulgtl0v

URL: [http://msviewer.ucsf.edu/prospector/cgi-bin/mssearch.cgi?report\\_title=MS-Viewer&search\\_key=kqlulgtl0v&search\\_name=msviewer](http://msviewer.ucsf.edu/prospector/cgi-bin/mssearch.cgi?report_title=MS-Viewer&search_key=kqlulgtl0v&search_name=msviewer)

#### *SMDC-treated Kp proteome*

Search key: lyibssyves

URL: [http://msviewer.ucsf.edu/prospector/cgi-bin/mssearch.cgi?report\\_title=MS-Viewer&search\\_key=lyibssyves&search\\_name=msviewer](http://msviewer.ucsf.edu/prospector/cgi-bin/mssearch.cgi?report_title=MS-Viewer&search_key=lyibssyves&search_name=msviewer)

## Results

### Culture model of antibiotic resistance

The *KpV513* isolate, which was a K2 capsular serotype, caused a severe multisystem disease that was unresponsive to cefazolin antimicrobial therapy. The infections reoccurred within the colony, suggesting a chronic carrier state for one or more of the individual animals. We examined tissue samples procured from an animal that presented multiple abscesses of the gastrointestinal tract and succumbed to infection by *KpV513*. Microscopic evaluation of cecum tissue revealed a significant bacterial burden (Fig. 1a) that was accompanied by the presence of numerous infiltrating macrophages (Supplemental Fig. S1). Ion intensity maps of infected cecum tissue, acquired by imaging mass spectrometry, exhibited marked increases in bacterial proteins that co-localized with *KpV513* observed microscopically (Fig. 1b and Supplemental Fig. S2). For example, the peptide at  $m/z = 1109.554$  (TLVQSTFADK) was detected from the acetylornithine/succinyl diaminepimelate aminotransferase ArgD of *KpV513*. The bacteria isolated from the infections exhibited a drug resistance profile (Supplemental Table S1) comparable to clinical extended-spectrum-beta-lactamase (ESBL)-*K. pneumoniae* isolates that are associated with fatal human infections. Mass spectrometry (Supplemental Table S2, S3) and genome sequencing (19) identified a Class A  $\beta$ -lactamase that was harbored by *KpV513*, which confirmed an ESBL designation for this strain.

We developed a culture model with *KpV513* to further examine responses of this invasive strain to antibiotics. In general, the expansion of bacterial populations can be described by four sequential phases: a lag with no detectable change ( $C_t$ ), the initial highest rate of expansion, a decaying rate of expansion, and a stationary phase of growth equilibrium that is limited by the carrying capacity of the culture environment. Because the minimum inhibitory concentration

(MIC) represents the drug level that completely blocks growth, 50% of the antibiotic MIC ( $MIC_{50}$ ) was used in broth cultures (Table 1). The reduced susceptibility to the penam (ampicillin) and cephem (cefazolin)  $\beta$ -lactams, as well as colistin, was obvious from growth attributes and MICs (Table 1). Interestingly, the growth curves for responses to each non- $\beta$ -lactam antibiotic demonstrated specific values for lengthened  $C_t$ , extended time to mid-exponential growth, and maximum cell density (Fig. 2a,b). Similar deviations from normal growth characteristics were also evident in the growth curves of clinical isolates of *E. coli*, *K. pneumoniae*, and *Acinetobacter baumannii*, as well as an attenuated strain of *Yersinia pestis*, that were treated with antibiotics at the  $MIC_{50}$  (Supplemental Table S1 and Supplemental Fig. S3). These results indicated that altered growth kinetics are a common response to antibiotics by Gram-negative bacteria, and are not specific to only *KpV513*. A discrete dynamical system method (20) was used to further examine the population responses of *KpV513* to antibiotics. For the initial phase of detectable growth in culture, we noted a decrease ( $39\% \pm 8.7\%$ ) in the rate of cell division with antibiotic treatment that directly correlated ( $R^2 = 0.95$ ) with  $C_t$  (Fig. 2c), and estimated that  $\sim 1.5\%$  ( $1.4\% \pm 0.36\%$ ) of total bacteria seeded tolerant cultures, regardless of the specific antibiotic. We observed no difference in cell size between untreated and antibiotic-treated *KpV513* by transmission electron microscopy (data not shown), indicating that the results represented actual population increases. Sampling cell density during the initial highest rate of expansion ( $M_{initial}$ ) and the decaying rate of expansion ( $M_{decay}$ ) provided an indication of the relationship between growth rate and the carrying capacity, which was influenced by the metabolic efficiency of carbon source conversions to biomass and the changing culture environment (pH, temperature, accumulation of toxic products, etc.) (21). Compared to untreated bacteria, antibiotic-treated cells exhibited shortened phases of growth rate decay that directly



correlated ( $R^2 = 0.89$ ) with reduced carrying capacity, indicating that antibiotic treatment reduced nutrient-to-biomass conversion efficiencies. For example, colistin treatment resulted in 10.4 hrs of growth-rate decay, which contributed to an additional population expansion that exceeded  $M_{initial}$  by  $> 50\%$ , while cultures treated with doxycycline exhibited a negligible growth decay phase that did not expand past  $M_{initial}$  (Table 1, Fig. 2d). Antibiotic-treated cells that were cultured with fresh antibiotic-free media reverted to the original drug susceptibility profiles (data not shown).

### **Drug-specific mechanisms of resistance**

Because the culture growth curves exhibited by antibiotic-treated bacteria appeared to be unique to each antibiotic (Fig. 2a-d), we reasoned that the proteome should display the steady-state composition of resistance, as measured by quantitative mass spectrometry (MS). We focused on the bactericidal streptomycin (SM) and bacteriostatic doxycycline (DC), which both impair protein synthesis by binding to the 16s rRNA component of the 30S ribosomal subunit, but differ in class (Table 1), structure (Fig. 3), and mechanism of transport across bacterial membranes. The MS analysis of untreated and antibiotic-treated cells expanded the experimental coverage of the 5,126 predicted bacterial gene products to 32% (1654), and included 614 open reading frames that encode orphan proteins predicted solely by gene annotation algorithms with no previous evidence of protein-level existence or known biochemical function (22). Antibiotic treatment resulted in substantial changes to the proteome that were reproducible across independently-cultured populations (Supplemental Fig. S4 and S5), and these global effects were also highly specific to each antibiotic (Fig. 2e), indicating transition from the steady-state control to new proteomic trajectories. As ribosomal function is the primary target of DC and SM, treated

bacteria should demonstrate alterations of the translational machinery that compensate for the toxic effects of these antibiotics. Compared to control and DC-treated bacteria, total ribosome content, quantitated as the average abundance of 54 ribosomal subunit proteins (109.3% of untreated for DC vs. 78.1% for SM), was significantly decreased (p-value < 0.00003) in SM-treated cells. Levels of the alarmones ppGpp and pppGpp ((p)ppGpp)), which influence protein allocation and control ribosomal synthesis (23, 24), are regulated by the activity of RelA and SpoT. RelA is recruited to stalled ribosomes where it converts GTP and ATP into pppGpp, while SpoT degrades ppGpp to GDP, releasing phosphate. We observed elevated levels of RelA for both DC and SM-treated cells, and increased (~2-fold) SpoT for DC-treated cells, suggesting a supportive role for alarmones in stabilizing the new proteomic trajectories. We further noted that bacteria that resisted SM, but not DC, exhibited substantially elevated levels of proteins that are transcriptionally regulated by alternative stress-response sigma factors (25) (Supplemental Fig. S6, Supplemental Table S2, S3). Sigma factors are multi-domain subunits of bacterial RNA polymerase that compete for binding to a limited number of holoenzymes, and have essential roles in promoter recognition and initiating steps of RNA synthesis.

### **Antibiotic transport**

We hypothesized that resistance should include off-target mechanisms because the antibiotics examined must first traverse the double membrane of Gram-negative bacteria and move through the cytoplasm before reaching the ribosomal targets. Intracellular transport of SM and similar aminoglycosides involves unknown receptors and requires a proton-motive force (PMF) that is driven by the aerobic electron transport chain (26), while DC requires porin channels that normally accommodate sugar carbon sources (27). Therefore, we examined changes to the

membrane that may limit intracellular transport of antibiotic. SM-treated bacteria exhibited elevated levels of fumarate reductase (FrdAB), which is transcriptionally activated under anaerobic conditions and reverses the tricarboxylic acid (TCA) cycle sequence from succinate to fumarate (28) (Fig. 3a and Supplemental Table S2, S3). Furthermore, SM-treated cells had increased abundance of the lysine decarboxylase CadA, which plays a role in pH homeostasis by consuming protons and neutralizing the acidic products of carbohydrate fermentation, as well as proteins (GhrAB, TrpC, KPN\_04670, KPN\_04772, YhbL, Tsa) involved in the conversion of reactive electrophilic species to non-reactive small carbon compounds. The 2-4 carbon acidic intermediates can enter central metabolism and contribute to diminished aminoglycoside susceptibility by decreasing PMF and TCA activity (29). In contrast to SM treatment, DC-treated bacteria had decreased abundance of the outer-membrane porins LamB (maltose) and OmpC (glucose), as well as the proteins MalE and MalM, which are required for maltose transport across the periplasmic space (Supplemental Table S2, S3). Because carbohydrate influx was likely to be dissimilar between SM- and DC-treated cells, we examined growth under aerobic or hypoxic conditions, using minimal medium with glucose as the sole carbon source. Accumulation of SM decreases under anaerobic metabolism (30), and SM-treated bacteria exhibited highly acidic culture supernatants (Supplemental Fig. S7a) resulting from an increased fermentative utilization of glucose (Supplemental Fig. S7b). Reduced antibiotic transport for DC-treated bacteria was a likely consequence of decreased glucose utilization (Supplemental Fig. S7b). Collectively, these results implicated a reduction in intracellular accumulation for both antibiotics.

### The proteomic transition to resistance

To compensate for changing membrane PMF or sugar permeability, downstream proteomic remodeling of central metabolic pathways was apparent in SM and DC-treated bacteria. Aligned with reduced import of sugars, resistance to DC involved a reduction in glycolytic enzymes (Fig. 3b and Supplemental Table S2, S3), while the TCA cycle was likely enhanced by the increased abundance of key enzymatic steps, mainly succinate dehydrogenase Sdh and malate dehydrogenase Mqo. In contrast to DC treatment, the increased gluconeogenesis and glycolytic enzymes observed in the SM-treated bacteria are essential for synthesis of glucose-6-phosphate from small carbon compounds as an alternative to C<sub>6</sub> sugars (31) (32), and it is possible that accelerated utilization of glucose compensated for the lower energy yield that resulted from a shift to anaerobic metabolism (Fig. 3a; Supplemental Fig. S7 and Supplemental Table S2, S3). Additionally, elevated levels of phosphoenolpyruvate synthesis enzymes suggested a necessity to breakdown the accumulated byproducts of fermentative metabolism, including C<sub>3</sub> and C<sub>4</sub> compounds or substrates that entered central metabolism via acetyl-CoA, such as acetate, fatty acids, and ethanol (33) (Fig. 3a and Supplemental Table S2, S3). We further observed increased prevalence of TCA cycle enzymes that do not require NAD<sup>+</sup> (PoxB, AcnA, and others) (Fig. 3a and Supplemental Table S2, S3). Preferential upregulation of TCA reactions that do not generate NADH will result in an increased ratio of intracellular NAD<sup>+</sup>/NADH, potentially leading to increased tolerance to bactericidal antibiotics due to decreased superoxide generation (34). Notably, reduced hydroxyl radical formation and elimination of H<sub>2</sub>O<sub>2</sub> induced by antibiotics was likely mediated by elevated levels of the bacterioferritin Bfr(35) and the DNA-binding protein from starved cells Dps (36, 37). Several components for turnover of arginine and histidine were

also elevated in SM-treated bacteria (Fig. 3a and Supplemental Table S2, S3). Curiously, ArgD of the arginine cycle was elevated in SM-treated cells, and this protein was also detected in tissues from infected monkeys (Fig. 1). Ammonia is the preferred nitrogen source of Gram-negative organisms, and it is possible that amino acid turnover leads to increased generation of this product (38).

The capsule of hypermucoviscous *K. pneumoniae* strains is a major virulence factor that provides protection from lethal serum factors and resistance to phagocytosis (39)(40). DC, but not SM, induced dramatically elevated levels of the capsule biosynthesis cluster (*cps*) encoded proteins GalF, Wza, and Wzi (Fig 3b and Supplemental Table S2, S3) that are required for polysaccharide export and stabilization. The *wzi* gene is found only in bacteria that assemble capsular polysaccharide (CPS) (41), and deletion of *wzi* from capsule-producing strains of *K. pneumoniae* results in decreased bacteria-associated CPS and increased secretion of CPS into the extracellular environment (40). Based on the changes in proteins for production and efflux of capsule, we anticipated an elevated level of capsular polysaccharide in DC-treated cells. Indeed, the DC-treated bacteria exhibited five-fold higher hypermucoviscosity compared to untreated cells (Supplemental Fig. S7), and presented a mesh-like network of polymers that protruded from outer cell membranes (Supplemental Fig. S8). Compared to DC-treated bacteria, CPS chains produced by untreated cells were shorter and loosely associated with the cell surface (Supplemental Fig. S8). In contrast to DC- and un-treated bacteria, no CPS was detectable in SM-treated cells (Supplemental Fig. S7c,S8b). Further, increased abundance of proteins encoded outside the *cps* locus that are necessary for production of CPS precursors indicated an extensive enhancement of the CPS synthesis pathway in DC-treated cells. This change included enzymes

for peptidoglycan synthesis and recycling (MurBC, Alr, and others), as well as proteins for generation of phosphoenolpyruvate (Fig. 3b).

### **Susceptibility to combination antibiotics**

Because resistance to SM resulted in unique biochemical pathways that were not likely to be compatible with DC resistance, we examined bacteria that were resistant to a combination of both antibiotics (SMDC). A novel proteome composition for dual antibiotic treatment was suggested by growth curves that were intermediate between those of individual drug treatment (Fig. 2f, Supplemental Table S2, S3). SMDC-treated cells comprised protein aspects that were in common with both drugs, as well as unique signatures (Fig 2e; Supplemental Fig. S5,S9), accounting for significant changes to 634 proteins. In all antibiotic treated cells, we observed elevated levels of proteins that link sulfur metabolism to cysteine biosynthesis and the “Cys/Cyss shuttle system” (CysABCDHIJKNP, Sbp, FliY; Fig. 3, Supplemental Fig. S9) that cycles cytoplasmic cysteine and periplasmic cystine to eliminate H<sub>2</sub>O<sub>2</sub> (42, 43). In comparing drug-specific mechanisms, SMDC-treated bacteria exhibited a decreased abundance of glucose import and utilization proteins (Gcd, OmpC, LamB, MalEM) that correlated with more aerobic utilization of glucose (Supplemental Fig. S7b). Levels of CPS export proteins (Wza and Wzi) were lower for SMDC than DC-treated bacteria, resulting in a proportionate reduction in synthesized CPS (Supplemental Fig. S7c,S8d). Specific SMDC signatures included decreased abundance of membrane proteins for the uptake of glycerol (GlpF), potassium (TrkA), and small molecules (OmpF), and increased abundance of the inner membrane proteins FtsK and ZipA, which are essential for cell division (Supplemental Fig. S9). Moreover, a unique mechanism to compensate for stalled translation in the dual drug treatment was suggested by elevated levels of the ribosome biogenesis GTPase RsgA that is essential to maturation of the 30S ribosomal

subunit and decreased abundance of the transcriptional repressor of methionine synthesis MetJ, which could increase initiation of translation (Supplemental Fig. S9).

We considered the possibility that proteomic remodeling boosts the ability of bacterial populations to survive successive exposure to the same antibiotic. Simulating antibiotic use in the clinic, we examined population responses of resistant bacteria that were re-treated with antibiotics at concentrations of 0.5-2.0 MIC. Figure 4 shows population expansion as a function of time and drug concentration. The addition of SM or DC to sensitive (untreated) cultures resulted in declining rates of replication and reduced carrying capacity that corresponded with increasing concentration of drug (Fig. 4a), whereas high doses of ampicillin ( $>60 \mu\text{g/mL}$ ) did not affect cell proliferation or maximum culture density of the resistant bacteria (Fig. 4b).

Remarkably, cultures of antibiotic-treated cells retreated with the same drug exhibited a resurgence in growth rates at concentrations  $> \text{MIC}$  that contributed to recovery of accumulated capacity with time (Fig. 4c,d), indicating an increase in drug-specific resistance. With SM-treatment, for example, the contour of low to high maximum culture capacity shifted vertically as the treatment dose of SM was increased (Fig. 4c), reflecting a shift to a higher level of resistance (Fig. 4b). However, we observed a horizontal collapse of SM-treated culture capacity with the addition of increasing concentrations of DC (Fig. 4c), indicating that sensitivity to DC was retained. Similarly, resistance to increasing concentrations of DC was exhibited by DC-treated bacteria (Fig. 4d), along with continued sensitivity to SM. Given the diversity of proteomic adaptations exhibited by SM- and DC-treated bacteria, it is likely that the drug-specific protective mechanisms established early in culture favored survival upon repeated exposure to the same drug. Interestingly, DC-treated cells exhibited decreased sensitivity to the highest treatment dose of SM (Fig. 4d), and after an extended lag phase ( $\sim 5$  hrs) the growth curve

resembled SM treatment more than DC treatment (data not shown), possibly due to the switch from DC- to SM-resistance.

## Discussion

The *K. pneumoniae* examined in our study harbors a plasmid-expressed  $\beta$ -lactamase that renders this bacterium resistant to most  $\beta$ -lactams, a class of antibiotics that contain a four-membered  $\beta$ -lactam ring that is structurally similar to the D-Ala-D-Ala moiety of the natural substrate(44). Growth of this ESBL isolate in response to non-carbapenem  $\beta$ -lactam antibiotics was identical to untreated controls (Fig. 2a,b), indicating that the toxic challenge was very efficiently resolved by  $\beta$ -lactamase activity. The antibiotics that we studied in detail have roughly the same mechanism of action but differ completely in chemical structure. SM is an aminoglycoside antibiotic that interacts with the small 16S rRNA of the 30S ribosomal subunit to inhibit binding of formyl-methionyl-tRNA(45), and the tetracycline class antibiotic DC inhibits binding of aminoacyl-tRNA to the mRNA-ribosome complex of the 30S subunit (46). The divergence between bacteria that grew in the presence of either DC or SM indicated that chemical structure was a primary driver of the global proteomic remodeling (Fig. 5). While retreatment of bacteria with the same antibiotic produced upward shifts in MICs, antibiotic treated cultures reverted to the original drug susceptibility profiles upon removal of antibiotic and culturing with fresh media, confirming the reversible nature of the proteomic remodeling (47, 48).

Instead of focusing on the first generation of surviving bacteria (49), we examined progeny cells that grew out from antibiotic-treated populations. Random precursors should have a selective advantage over the rest of the population, and these bacteria expand in number to rapidly overtake less fit bacteria. By starting cultures with approximately 200 bacteria that were



synchronized in replication, we minimized the possible contribution of dormant and dying cells or chemical communication between cells. A framework was recently proposed (49) for classifying the drug response of bacterial strains by measurement of the MIC together with a quantitative indicator of tolerance, the minimum duration for killing (MDK). The reported range for tolerant precursors based on the MDK is 0.001 - 10% (50), while ~1.5% of the bacterial population in our model give rise to resistant bacteria. Instead of a stable metric, it is conceivable that the frequency of precursors represents the inherent heterogeneity of the total bacterial population or the multiple distinct cellular physiologies within a population (51). Disproportionate partitioning of the proteome (52, 53) or (p)ppGpp-like signaling molecules in daughter cells during replication as a bet-hedging strategy will ensure fitness of the overall population in unstable environments.

Compared to single antibiotic efficacy, combination therapies attempt to use antibiotics with independent mechanisms of action, generally a  $\beta$ -lactam and an aminoglycoside. Combining two or more antibiotics as a treatment option can result in additive and synergistic activities that potentially reduce the likelihood of the emergence of resistant bacteria, while antagonistic effects may lower efficacy. However, selecting antibiotics for the most efficacious combination therapy is empirical (54) or based on trial and error. Adjusting the chemical properties of antibiotics to improve accumulation within Gram-negative pathogens can convert ineffective compounds into highly active antimicrobials (55). In a similar manner, proteomic adjustments of the bacteria responding to one antibiotic can alter antibiotic properties of a second compound. From our results, resistance to combination treatment with two antibiotics was mediated by both drug-specific and unique mechanisms (Fig. 5), perhaps because some components of the remodeled proteomes that were necessary for survival in the presence of a one

drug may increase susceptibility to the other drug. These results further suggest that antibiotics with similar molecular targets but different chemical structures may be useful for combination therapies if used under conditions that do not promote resistance.

## References

1. Struve C, Bojer M, & Krogfelt KA (2008) Characterization of *Klebsiella pneumoniae* type 1 fimbriae by detection of phase variation during colonization and infection and impact on virulence. *Infect Immun* 76(9):4055-4065.
2. Struve C, Bojer M, & Krogfelt KA (2009) Identification of a conserved chromosomal region encoding *Klebsiella pneumoniae* type 1 and type 3 fimbriae and assessment of the role of fimbriae in pathogenicity. *Infect Immun* 77(11):5016-5024.
3. Paczosa MK & Meccas J (2016) *Klebsiella pneumoniae*: Going on the Offense with a Strong Defense. *Microbiol Mol Biol Rev* 80(3):629-661.
4. Gu D, *et al.* (A fatal outbreak of ST11 carbapenem-resistant hypervirulent *Klebsiella pneumoniae* in a Chinese hospital: a molecular epidemiological study. *The Lancet Infectious Diseases*.
5. Burke RL, Whitehouse CA, Taylor JK, & Selby EB (2009) Epidemiology of invasive *Klebsiella pneumoniae* with hypermucoviscosity phenotype in a research colony of nonhuman primates. *Comparative medicine* 59(6):589-597.
6. Twenhafel NA, *et al.* (2008) Multisystemic abscesses in African green monkeys (*Chlorocebus aethiops*) with invasive *Klebsiella pneumoniae*--identification of the hypermucoviscosity phenotype. *Veterinary pathology* 45(2):226-231.
7. Blango MG & Mulvey MA (2010) Persistence of uropathogenic *Escherichia coli* in the face of multiple antibiotics. *Antimicrob Agents Chemother* 54(5):1855-1863.
8. Claudi B, *et al.* (2014) Phenotypic variation of *Salmonella* in host tissues delays eradication by antimicrobial chemotherapy. *Cell* 158(4):722-733.
9. Livermore DM (2009) Has the era of untreatable infections arrived? *J Antimicrob Chemother* 64 Suppl 1:i29-36.
10. Amato SM, Orman MA, & Brynildsen MP (2013) Metabolic control of persister formation in *Escherichia coli*. *Mol Cell* 50(4):475-487.
11. Shan Y, *et al.* (2017) ATP-Dependent Persister Formation in *Escherichia coli*. *MBio* 8(1).
12. Andrews JM (2001) Determination of minimum inhibitory concentrations. *J Antimicrob Chemother* 48 Suppl 1:5-16.
13. Fang CT, Chuang YP, Shun CT, Chang SC, & Wang JT (2004) A novel virulence gene in *Klebsiella pneumoniae* strains causing primary liver abscess and septic metastatic complications. *J Exp Med* 199(5):697-705.
14. Wisniewski JR, Zougman A, Nagaraj N, & Mann M (2009) Universal sample preparation method for proteome analysis. *Nat Methods* 6(5):359-362.
15. Rappsilber J, Mann M, & Ishihama Y (2007) Protocol for micro-purification, enrichment, pre-fractionation and storage of peptides for proteomics using StageTips. *Nat Protoc* 2(8):1896-1906.

16. Lazar C, Gatto L, Ferro M, Bruley C, & Burger T (2016) Accounting for the Multiple Natures of Missing Values in Label-Free Quantitative Proteomics Data Sets to Compare Imputation Strategies. *J Proteome Res* 15(4):1116-1125.
17. Webb-Robertson BJ, *et al.* (2015) Review, evaluation, and discussion of the challenges of missing value imputation for mass spectrometry-based label-free global proteomics. *J Proteome Res* 14(5):1993-2001.
18. Vizcaino JA, *et al.* (2014) ProteomeXchange provides globally coordinated proteomics data submission and dissemination. *Nat Biotechnol* 32(3):223-226.
19. Holt KE, *et al.* (2015) Genomic analysis of diversity, population structure, virulence, and antimicrobial resistance in *Klebsiella pneumoniae*, an urgent threat to public health. *Proc Natl Acad Sci U S A* 112(27):E3574-3581.
20. Johnson ASA, Madden KM, & Şahin AA (2017) *Discovering Discrete Dynamical Systems* (MATHEMATICAL ASSN AMERICA).
21. Reding-Roman C, *et al.* (2017) The unconstrained evolution of fast and efficient antibiotic-resistant bacterial genomes. 1:0050.
22. Suh MJ, Keasey SL, Brueggemann EE, & Ulrich RG (2017) Antibiotic-dependent perturbations of extended spectrum beta-lactamase producing *Klebsiella pneumoniae* proteome. *Proteomics* 17(9).
23. Potrykus K & Cashel M (2008) (p)ppGpp: still magical? *Annu Rev Microbiol* 62:35-51.
24. Lemke JJ, *et al.* (2011) Direct regulation of *Escherichia coli* ribosomal protein promoters by the transcription factors ppGpp and DksA. *Proc Natl Acad Sci U S A* 108(14):5712-5717.
25. Seo JH, *et al.* (2012) Multiple-omic data analysis of *Klebsiella pneumoniae* MGH 78578 reveals its transcriptional architecture and regulatory features. *BMC Genomics* 13:679.
26. Taber HW, Mueller JP, Miller PF, & Arrow AS (1987) Bacterial uptake of aminoglycoside antibiotics. *Microbiol Rev* 51(4):439-457.
27. Chopra I & Roberts M (2001) Tetracycline antibiotics: mode of action, applications, molecular biology, and epidemiology of bacterial resistance. *Microbiol Mol Biol Rev* 65(2):232-260 ; second page, table of contents.
28. Cecchini G, Schröder I, Gunsalus RP, & Maklashina E (2002) Succinate dehydrogenase and fumarate reductase from *Escherichia coli*. *Biochimica et Biophysica Acta (BBA) - Bioenergetics* 1553(1):140-157.
29. Meylan S, *et al.* (2017) Carbon Sources Tune Antibiotic Susceptibility in *Pseudomonas aeruginosa* via Tricarboxylic Acid Cycle Control. *Cell chemical biology* 24(2):195-206.
30. Kogut M, Lightbrown JW, & Isaacson P (1965) Streptomycin Action and Anaerobiosis. *J Gen Microbiol* 39:155-164.
31. Bologna FP, Andreo CS, & Drincovich MF (2007) *Escherichia coli* malic enzymes: two isoforms with substantial differences in kinetic properties, metabolic regulation, and structure. *J Bacteriol* 189(16):5937-5946.
32. Eydallin G, *et al.* (2010) Genome-wide screening of genes whose enhanced expression affects glycogen accumulation in *Escherichia coli*. *DNA Res* 17(2):61-71.
33. Spaans SK, Weusthuis RA, van der Oost J, & Kengen SW (2015) NADPH-generating systems in bacteria and archaea. *Front Microbiol* 6:742.
34. Kohanski MA, Dwyer DJ, Hayete B, Lawrence CA, & Collins JJ (2007) A common mechanism of cellular death induced by bactericidal antibiotics. *Cell* 130(5):797-810.

35. Crow A, Lawson TL, Lewin A, Moore GR, & Le Brun NE (2009) Structural basis for iron mineralization by bacterioferritin. *J Am Chem Soc* 131(19):6808-6813.
36. Bradley JM, *et al.* (2015) Three Aromatic Residues are Required for Electron Transfer during Iron Mineralization in Bacterioferritin. *Angew Chem Int Ed Engl* 54(49):14763-14767.
37. Bellapadrona G, Ardini M, Ceci P, Stefanini S, & Chiancone E (2010) Dps proteins prevent Fenton-mediated oxidative damage by trapping hydroxyl radicals within the protein shell. *Free Radic Biol Med* 48(2):292-297.
38. Bender RA (2010) A NAC for regulating metabolism: the nitrogen assimilation control protein (NAC) from *Klebsiella pneumoniae*. *J Bacteriol* 192(19):4801-4811.
39. Hsu CR, Lin TL, Chen YC, Chou HC, & Wang JT (2011) The role of *Klebsiella pneumoniae* rmpA in capsular polysaccharide synthesis and virulence revisited. *Microbiology* 157(Pt 12):3446-3457.
40. Alvarez D, Merino S, Tomas JM, Benedi VJ, & Alberti S (2000) Capsular polysaccharide is a major complement resistance factor in lipopolysaccharide O side chain-deficient *Klebsiella pneumoniae* clinical isolates. *Infect Immun* 68(2):953-955.
41. Bushell SR, *et al.* (2013) Wzi is an outer membrane lectin that underpins group 1 capsule assembly in *Escherichia coli*. *Structure* 21(5):844-853.
42. Ohtsu I, *et al.* (2015) Uptake of L-cystine via an ABC transporter contributes defense of oxidative stress in the L-cystine export-dependent manner in *Escherichia coli*. *PLoS One* 10(3):e0120619.
43. Ohtsu I, *et al.* (2010) The L-cysteine/L-cystine shuttle system provides reducing equivalents to the periplasm in *Escherichia coli*. *J Biol Chem* 285(23):17479-17487.
44. Tipper DJ & Strominger JL (1965) Mechanism of action of penicillins: a proposal based on their structural similarity to acyl-D-alanyl-D-alanine. *Proc Natl Acad Sci U S A* 54(4):1133-1141.
45. Sharma D, Cukras AR, Rogers EJ, Southworth DR, & Green R (2007) Mutational analysis of S12 protein and implications for the accuracy of decoding by the ribosome. *J Mol Biol* 374(4):1065-1076.
46. Geigenmuller U & Nierhaus KH (1986) Tetracycline can inhibit tRNA binding to the ribosomal P site as well as to the A site. *Eur J Biochem* 161(3):723-726.
47. Dou H, Jiang M, Peng H, Chen D, & Hong Y (2003) pH-dependent self-assembly: micellization and micelle-hollow-sphere transition of cellulose-based copolymers. *Angew Chem Int Ed Engl* 42(13):1516-1519.
48. Lewis K (2010) Persister cells. *Annu Rev Microbiol* 64:357-372.
49. Balaban NQ, Merrin J, Chait R, Kowalik L, & Leibler S (2004) Bacterial persistence as a phenotypic switch. *Science* 305(5690):1622-1625.
50. Hofsteenge N, van Nimwegen E, & Silander OK (2013) Quantitative analysis of persister fractions suggests different mechanisms of formation among environmental isolates of *E. coli*. *BMC Microbiol* 13:25.
51. Allison KR, Brynildsen MP, & Collins JJ (2011) Heterogeneous bacterial persisters and engineering approaches to eliminate them. *Curr Opin Microbiol* 14(5):593-598.
52. Bergmiller T, *et al.* (2017) Biased partitioning of the multidrug efflux pump AcrAB-TolC underlies long-lived phenotypic heterogeneity. *Science* 356(6335):311-315.
53. Rego EH, Audette RE, & Rubin EJ (2017) Deletion of a mycobacterial divisome factor collapses single-cell phenotypic heterogeneity. *Nature* 546(7656):153-157.

54. Kumar A, *et al.* (2010) Early combination antibiotic therapy yields improved survival compared with monotherapy in septic shock: a propensity-matched analysis. *Crit Care Med* 38(9):1773-1785.
55. Richter MF, *et al.* (2017) Predictive compound accumulation rules yield a broad-spectrum antibiotic. *Nature* 545(7654):299-304.

**Figure 1. *Klebsiella pneumoniae* infection in the large intestine of a *Chlorocebus aethiops* *sabaeus* monkey.** Evaluation of cecum tissue procured during necropsy of a subject that presented multiple abscesses of the gastrointestinal tract and succumbed to *K. pneumoniae* infection. **(a)** Immunofluorescence to detect nuclei (blue) and *K. pneumoniae* cells (green). **(b)** Collection of ion intensity for the *K. pneumoniae* peptide at  $m/z$  1109.554 Da from imaging mass spectrometry. The peptide from aminotransferase ArgD protein co-localized with *K. pneumoniae* cells detected by immunofluorescence in (a).

**Figure 2. Growth of *Klebsiella pneumoniae* in response to antibiotics that target cell wall synthesis or ribosomal function.** Extended spectrum  $\beta$ -lactamase-producing *K. pneumoniae* were cultured untreated (black), with ampicillin (gray) at the highest tested dose (128  $\mu$ g/mL), or in the presence of susceptible antibiotics at the MIC<sub>50</sub>. **(a)** Culture growth curves and **(b)** rates of replication based on first derivative growth curves, overlaid from the time of detectable increases in culture absorbance. **(c)** Relationship between the initial rate of replication and time to detectable increase in optical density in early culture. **(d)** Relationship between culture density accumulated during the decay phase of growth and the relative culture capacity that was normalized to the maximum capacity attained at the highest replication rates during the initial phase of growth ( $M_{initial}$ ). **(e)** Principal component analysis of proteins identified by mass spectrometry, for all biological replicates (closed circles) of each treatment condition: streptomycin, SM; doxycycline, DC; combination of SM and DC, SMDC; untreated. **(f)** Culture growth and replication rates (inset) of bacteria tolerant to ribosomal synthesis inhibitors. Coloring is consistent throughout: cefazolin, orange; meropenem, pink; colistin, cyan;

streptomycin, blue; doxycycline, red; chloramphenicol, purple; combination of streptomycin and doxycycline, green.

**Figure 3. Antibiotic-specific biochemical pathways of resistance.** Proteins that exhibited significant changes in abundance ( $\pm 2$ -fold compared to untreated cells;  $p$ -value  $< 0.05$ ) in (a) streptomycin or (b) doxycycline-treated cells were mapped to molecular pathways by functional network associations (glycolysis, green; transcription and translation, gray; removal of reactive oxygen species (ROS), red; iron-sulfur (Fe-S) cluster biogenesis, blue; nitrogen cycle, tan; fatty acid biosynthesis, purple; arginine cycle, pink; tricarboxylic acid (TCA) cycle, yellow, capsular polysaccharide (CPS) biosynthesis, orange). Regulation of pathway reactions by proteins exhibiting unchanged (black vector), increased (green vector), or decreased (red segment) abundance. Selected cellular proteins are designated by shape: outer membrane porins (oval dimers), components involved in electron transport (pentagon), protein synthesis (oval), or removal of ROS (circle). The protein color is identical for pathway regulation that is common to both antibiotics, and subdued with red dashed borders if down-regulated in one treatment versus the other.

**Figure 4. Proteomic remodeling boosts survival during successive exposures to the same antibiotic.** Cultures of (a) untreated, (b) ampicillin resistant, (c) streptomycin treated, and (d) doxycycline treated extended spectrum  $\beta$ -lactamase-producing *K. pneumoniae* were treated with streptomycin (left column), doxycycline (middle column), or ampicillin (right), using 0.5-2x the minimum inhibitory concentration. Low (blue) to high (red) accumulated culture density; slow (gray) to fast (black) replication rate.

**Figure 5. Activated proteomic compartments of bacteria that are resistant to antibiotics targeting the ribosome.** (a) Susceptible bacteria treated with streptomycin or doxycycline; (b) Decreased susceptibility to streptomycin, (c) doxycycline, or (d) the combination of streptomycin and doxycycline, showing mechanisms that are shared with streptomycin (blue) or doxycycline (orange), or common to both antibiotics (green).



## Tables

Table 1. Growth response of *Klebsiella pneumoniae* to antibiotic treatment.

Treatment <sup>a</sup>	Class	Mechanism Bacteri-	Target	MIC (µg/mL)	Lag (Ct, hr)	Doubling time (min)	$M_{initial}$ (A <sub>260</sub> )	$M_{decay}$ (A <sub>260</sub> )	Growth decline (hr)
Untreated					3.71	21.40	0.86	1.32	12
Ampicillin*	Penicillin	cidal	Cell wall	>128	3.37	21.79	0.87	1.29	12
Cefazolin*	Cephalosporin	cidal	Cell wall	4	4.20	30.61	0.77	1.39	14.2
Meropenem	Carbapenem	cidal	Cell wall	1	15.16	69.25	0.85	1.25	11.1
Colistin*	Polymyxin	cidal	Cell wall	4	6.65	25.65	0.85	1.32	10.4
Streptomycin	Aminoglycosid	cidal	30S ribosome	4	7.34	31.84	0.99	1.13	6.5
Doxycycline	Tetracycline	ostatic	30S ribosome	1	6.35	26.08	2.40	1.00	14.8
Chloramphenicol*	Amphenicol	ostatic	50S ribosome	16	12.58	79.24	0.93	1.14	8.5

<sup>a</sup>Growth properties determined at the antibiotic MIC<sub>50</sub>

\*MIC indicates resistance (ampicillin) and reduced susceptibility (cefazolin, colistin, chloramphenicol).

## Figures

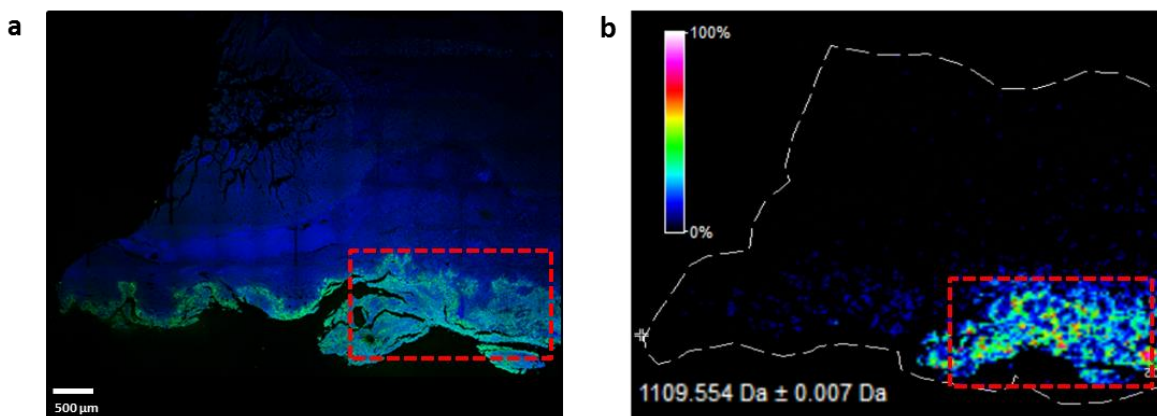


Figure 1.

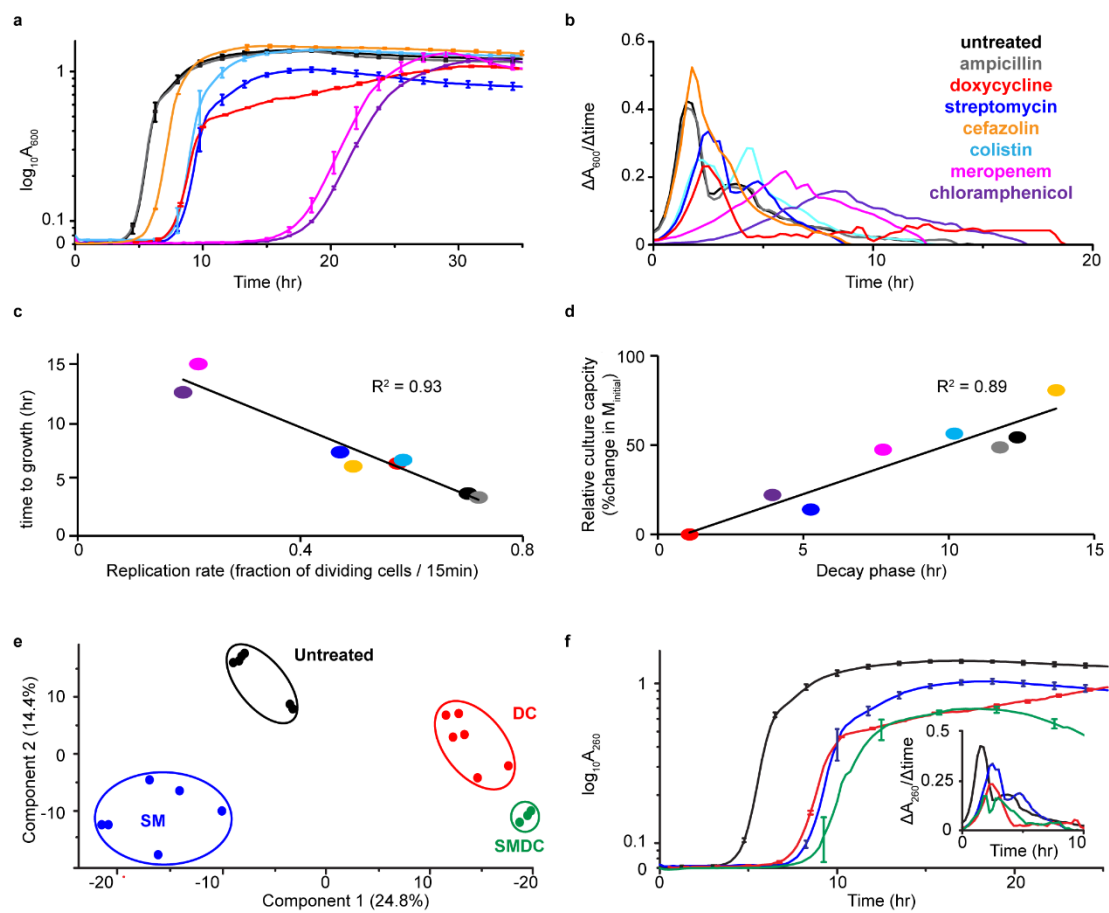


Figure 2.

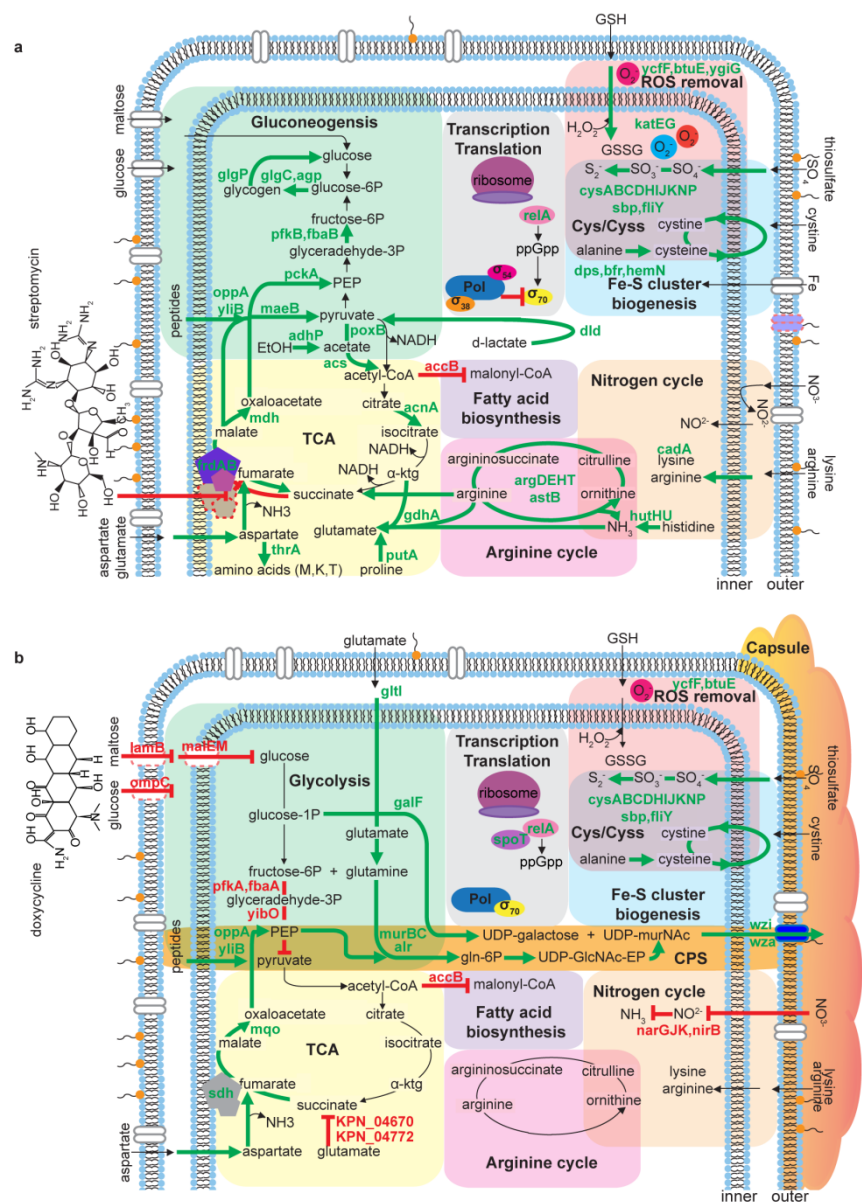


Figure 3.

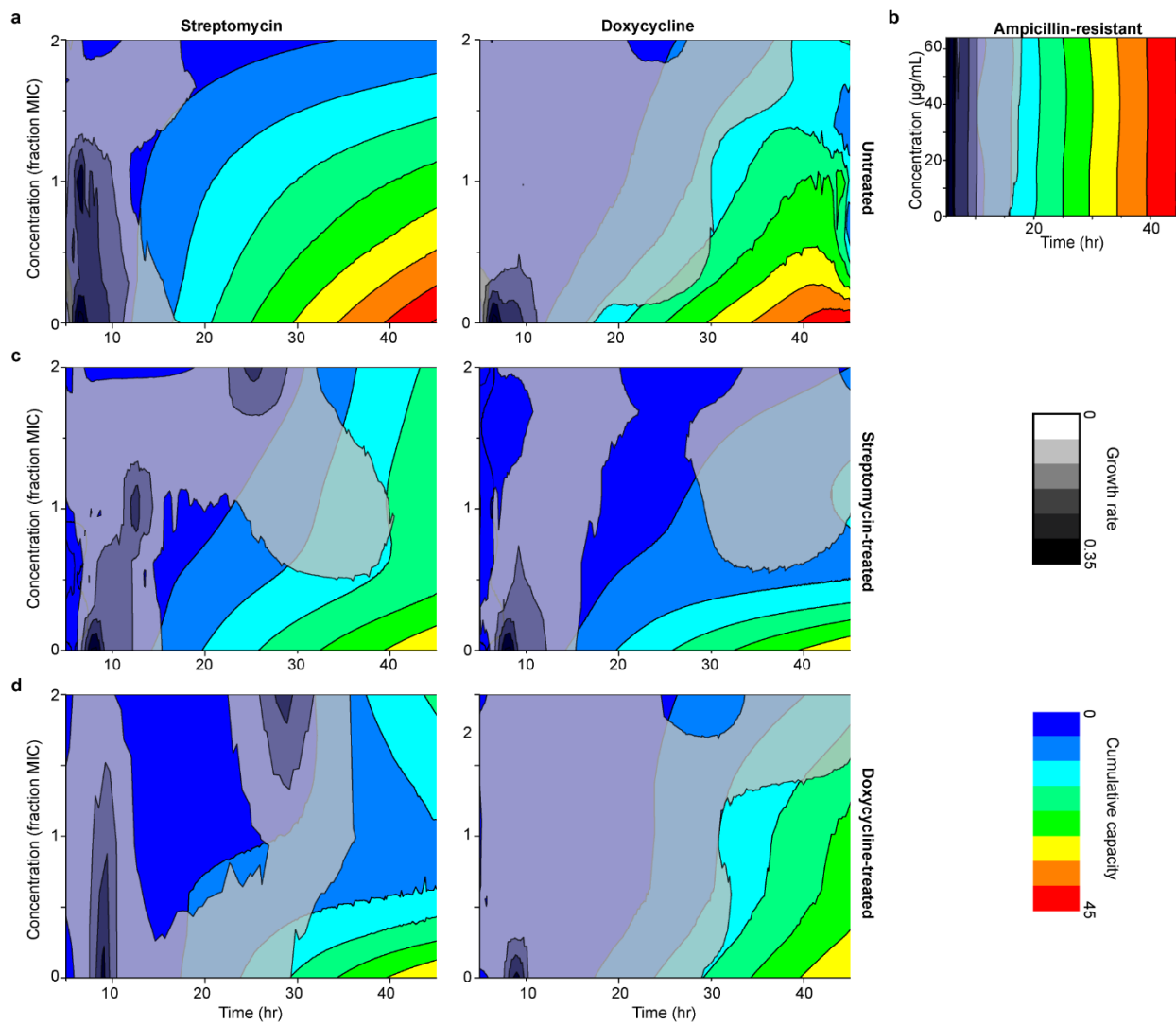


Figure 4.

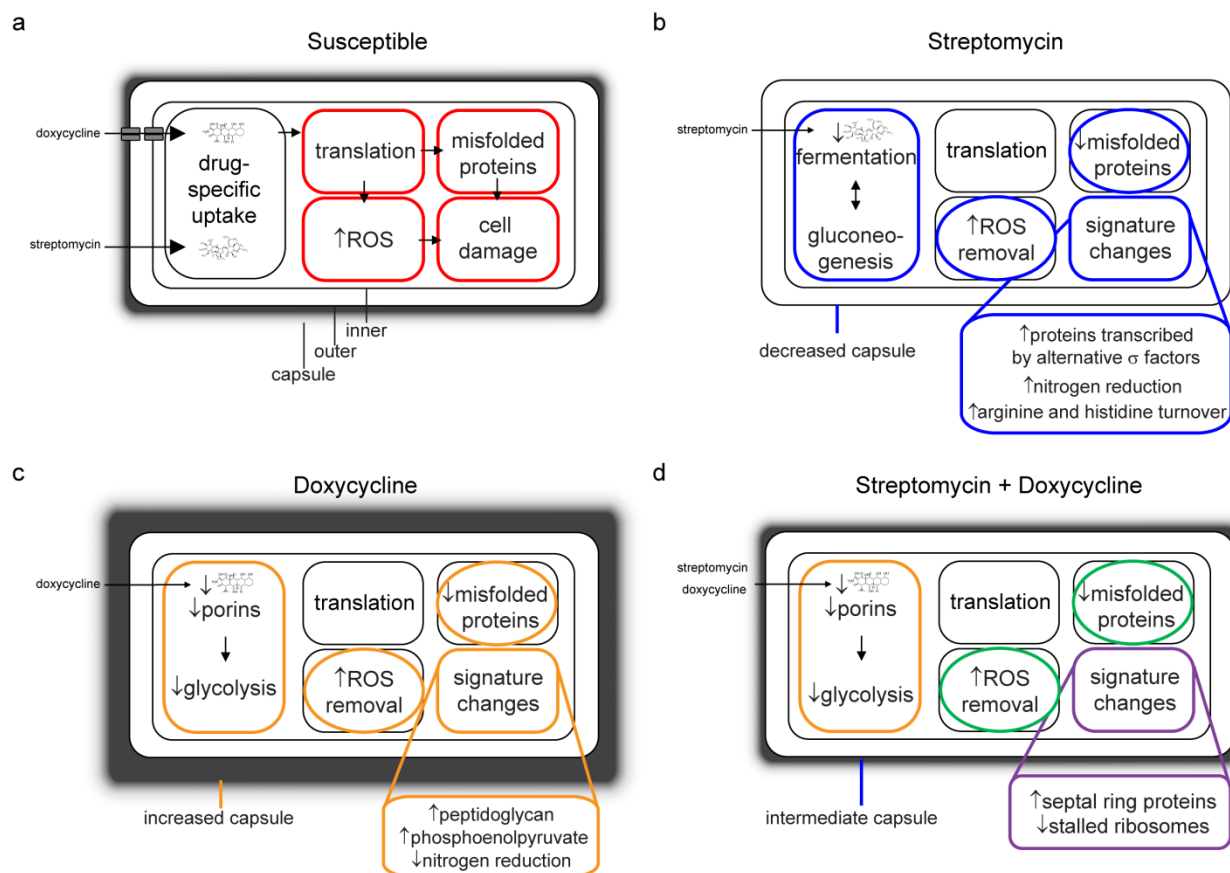


Figure 5.